Progress In Electromagnetics Research M, Vol. 139, 21–35, 2026

PIER M

(Received 18 March 2026, Accepted 13 May 2026, Scheduled 27 July 2026)

Modulation of Electromagnetic Wave Physical Characteristics by Strongly Anisotropic Acoustic Metamaterials

Zhanying Guo*, Hui Li, and Yang An

Jiaozuo Normal College, Jiaozuo 454000, China

ABSTRACT: Objective: This study aims to experimentally and numerically investigate the modulation of electromagnetic wave physical characteristics (transmittance, absorptance, impedance) by strongly anisotropic acoustic metamaterials in the 2–12 GHz frequency band, and to quantify the influence of material parameters (thickness, density, elastic modulus, anisotropic direction) on wave control performance. **Methods:** Three types of material units (metal composite, polymer, ceramic reinforced) with thicknesses of 1.5–3 mm and anisotropic directions along X, Y, Z axes were fabricated. Transmittance and absorbance were measured using a vector network analyzer with a WR-90 guideway system. Finite element simulations incorporating acoustic-electromagnetic coupling (strain-induced permittivity modulation) were conducted. Sensitivity analysis was performed by varying thickness (±10%), elastic modulus (±5 GPa), density (±500 kg/m^3), and direction angle (±15°). **Results:** High-frequency absorbance reached 0.91 (metal composite at 9.5 GHz), while low-frequency transmittance remained above 0.70. Thickness and elastic modulus predominantly affected the amplitude and position of high-frequency absorption peaks, whereas density and direction angle primarily regulated low-frequency response, resulting in multi-peak broadband absorption. The deviation between experimental data and finite element simulation was less than 3%. Sensitivity analysis revealed that thickness (±10%) and elastic modulus (±5 GPa) produced the most significant changes in transmittance (0.60–0.91) and absorptance (0.70–0.91). **Conclusion:** Strongly anisotropic acoustic metamaterials offer mechanically tunable electromagnetic wave control, with thickness and elastic modulus as key design parameters. These findings provide experimental and theoretical references for high-frequency communication antennas, radar stealth coatings, and broadband absorption devices.

1. INTRODUCTION

Acoustic metamaterials are artificially designed structural unit combinations that show wave characteristics that traditional materials cannot achieve. Anisotropic acoustic metamaterials show highly direction-dependent elastic modulus and density distribution by adjusting material parameters in different directions. Such materials show complex coupling characteristics in the field of electromagnetic wave control, such as enhanced frequency dependence of transmission, reflection, and absorption. In the fields of radar absorption, communication antennas, and acoustic-optic devices, such materials can provide a wider bandwidth response and a stronger wave resistance matching effect than conventional materials. Fine design of anisotropic structure can reduce the transmittance to below 0.65 and the absorption rate to above 0.9 in the frequency band from 2 to 12 GHz. Studying this kind of material can not only enrich electromagnetic wave physics theory but also guide the development of new functional devices and provide experimental data support for the wave-control design of high-frequency electronic systems.

The scientific bottleneck lies in the fact that conventional electromagnetic absorbers and metamaterials achieve tunability only through geometric patterning or material composition, which are fixed after fabrication. In contrast, acoustic metamaterials exploit elastic anisotropy as a post-fabrication adjustable parameter. However, the direct coupling between acoustic vibrations and GHz electromagnetic waves remains unexplored, and no existing work quantifies how anisotropic elastic constants modulate transmittance/absorbance in the 2–12 GHz band.

Unlike conventional electromagnetic metamaterials that rely solely on permittivity/permeability engineering, strongly anisotropic acoustic metamaterials offer a unique advantage: their elastic modulus and density can be directionally tailored, enabling mechanical-field reconfiguration of electromagnetic responses. This provides a new degree of freedom for wave control, particularly for adaptive radar stealth and communication antennas where real-time tuning is desired.

The existing works have demonstrated various applications of acoustic metamaterials in noise control, underwater acoustics, and multi-physics cloaking. However, none of them have experimentally investigated the direct modulation of GHz electromagnetic waves using strongly anisotropic acoustic metamaterials, nor have they quantified how elastic anisotropy parameters (modulus, density, direction) affect transmittance and absorbance in the 2–12 GHz band. This gap motivates our study: to experimentally validate whether acoustic anisotropy can serve as an effective tuning knob for electromagnetic wave control and to provide a parametric basis for future hybrid acoustic-electromagnetic devices.

The research on acoustic metamaterials has developed rapidly in recent years, involving structural design, wave

* Corresponding author: Zhanying Guo (guo7011@126.com).

control mechanisms, and multi-physics field coupling. Yao et al. commented on the application and challenges of acoustic metamaterials and pointed out that the anisotropic structure of materials can adjust the sound wave propagation in lightweight noise control in large-scale transportation environments, and there are still engineering limitations in complex structural design and large-scale application [1]. Liu et al. prepared composite microspheres with a raspberry structure, which enhanced the attenuation of electromagnetic waves, indicating that controlling the exothermic process can finely adjust the internal microstructure of materials and realize frequency-selective wave energy dissipation [2]. Cao et al. studied the strength anisotropy and rotation anisotropy in the stability of clay slope and showed the remarkable influence of anisotropy on mechanical response, which provided a theoretical basis for multi-directional regulation [3]. Li et al. proposed a multi-channel absorption compensation method to achieve stable recovery of high-frequency components, emphasizing the ability to regulate multi-band signals [4]. Cui et al. put forward a polarization control operator, designed polarized electromagnetic waves, and demonstrated the contractility of materials on electromagnetic-wave directive and polarization [5].

Wan et al. improved the magnetic loss and impedance matching through a laminated structure and achieved a balance in low/high-frequency broadband microwave absorption. The structural combination can optimize the frequency response of materials [6]. Kim et al. used finite element analysis to verify the bearings of wind turbines, and the finite element modeling in complex mechanical systems provided a method reference [7]. Liu et al. adopted multiple physical zero media to realize thermal and electromagnetic shielding at the same time, which shows that the coupling design of multiple physical fields can play a role in frequency regulation and energy transmission [8]. He et al. put forward the method of multi-physics field and zero medium to realize the simultaneous control of electromagnetic wave and heat flow, and expand the theoretical model of multi-functional regulation of materials [9]. Lu et al. studied the simplified tire finite element modeling method, provided the scheme of structural parameter optimization and calculation efficiency, and provided reference for complex material simulation [10].

Chen and Huang combined penetrating manipulation with acoustic metamaterials to realize acoustic stealth design, emphasizing the influence of microstructure arrangement on acoustic shielding [11]. Liu et al. put forward the magneto-electric integrated design strategy of NiCo@C composites, including medium and high-frequency microwave absorption and energy conversion, which demonstrated the ability of composite materials to adjust and control multi-band wave energy [12]. Dong et al. studied underwater acoustic metamaterials and analyzed the control mechanism of sound wave propagation in the water environment, providing experimental and theoretical bases for the application of anisotropic structures in complex media [13]. The existing research covers the microstructure design, anisotropic control, electromagnetic/acoustic coupling, and multi-physics field application, showing a comprehensive development trend from a theoretical model to experimental verification and from low frequency to high frequency, which provides a solid foundation for the application of acoustic metamaterials in electromagnetic wave control and absorption.

Recent works on near-zero-index media achieve electromagnetic cloaking via multi-physical null media, while photogenic doping controls polarization states. Thermal metamaterials address heat-flow modulation but lack GHz-frequency electromagnetic response. Compared with these approaches, our work fills a distinct gap: using acoustic anisotropy to modulate electromagnetic waves. No prior study has experimentally linked directional elastic modulus (1–15 GPa) and density (1200–7800 kg/m^3) to transmittance/absorbance in the 2–12 GHz band. Thus, the incremental contribution is the demonstration of an acoustic-electromagnetic tuning mechanism that is orthogonal to existing electromagnetic-only or thermal-only designs.

This paper focuses on the application performance of strongly anisotropic acoustic metamaterials in electromagnetic-wave regulation, the comparison between target experiments and simulations, and the quantification of the effects of different structural parameters on transmittance, absorption rate, and wave impedance. We designed a variety of material combinations, including metal composite, polymer, and ceramic reinforcement units. We then constructed two-dimensional and three-dimensional anisotropic models, and measured them in 2–12 GHz frequency band. Combined with finite element simulation and a parameter optimization algorithm, the adjustment ability of thickness, density, elastic modulus, and anisotropic direction to wave characteristics is evaluated. Identify the best combination of different parameter configurations in a specific frequency band, provide data basis and theoretical support for future communication antenna design, radar stealth and broadband absorption device development, and verify the consistency between experimental results and model prediction.

Research methods include experimental measurement, numerical simulation, and sensitivity analysis. In the experimental part, the prepared anisotropic metamaterial samples are used to measure the transmittance and absorptivity in the range of 2 to 12 GHz, and the impedance changes of the materials in different directions are recorded. In the simulation part, the finite element model is constructed; the material density, elastic modulus, and anisotropy parameters are input; and the transmission loss is calculated by the wave equation and electromagnetic coupling boundary conditions. Parameter sensitivity analysis imperatively optimizes different thickness and material parameters through the least squares objective function, and quantifies the contribution of each parameter to the fluctuation characteristics. The normalization of data processing and elimination of abnormal values ensure the comparability of simulated and experimental data and generate parameter-performance curves and comparison charts, which provide a basis for structural design and practical application.

Compared with conventional multilayer dielectrics or anisotropic electromagnetic absorbents, our work does not claim a breakthrough in absolute absorption bandwidth. Instead, we introduce a distinct tuning mechanism: the

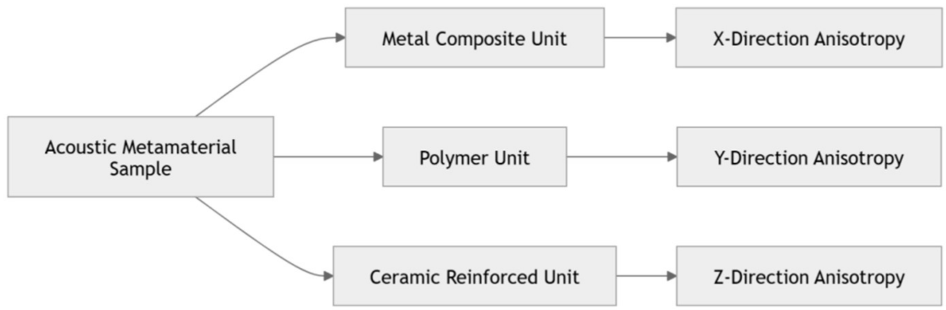

FIGURE 1. Schematic diagram of experimental samples of acoustic metamaterials.

TABLE 1. Experimental sample parameters.

Sample number	Material Type	Thickness (mm)	Unit density (kg/m)	Elastic modulus (GPa)	Anisotropic direction
S1	Metal composite	2.5	7800	10	X axis
S2	Polymer	3.0	1200	2	Y axis
S3	pottery and porcelain	1.5	3800	15	Z axis

strong elastic anisotropy of the acoustic metamaterial enables reconfiguration control of electromagnetic wave transmittance and absorbance via mechanical parameters (thickness, elastic modulus, direction angle) rather than solely through electromagnetic geometry. This offers an additional degree of freedom for wave manipulation, particularly in scenarios where electromagnetic design is constrained.

2. MATERIALS AND METHODS

2.1. Data Collection and Sample Selection

2.1.1. Data Sources and Collection Methods

The experimental samples are metal composite, polymer, and ceramic reinforcement units, and the preparation of the samples is based on two-dimensional and three-dimensional anisotropic structure designs. The sample data come from self-preparation and previous laboratory measurement results, and the collection range covers the material combination with a thickness of 1.5 to 3 mm and a unit period of 5 to 20 mm. The electromagnetic wave experiment was conducted in 2–12 GHz frequency band. The transmittance, absorptivity, and wave impedance of each sample in X, Y, and Z directions were measured, and the frequency, amplitude, and ambient temperature of each measurement were recorded (controlled at $23 \pm 1°$C). The data acquisition adopts the interface between the Vector Network Analyzer (VNA) and the standard waveguide to ensure the repeatability of the test. All measured data are saved in CSV format, which is convenient for subsequent numerical processing and simulation comparison.

Figure 1 shows the arrangement structure of three types of material units in the anisotropic direction, which clarifies the design logic and acquisition dimensions of experimental samples. The main node represents the acoustic metamaterial sample used in experiments. Sub-nodes indicate the three types of material units: Metal Composite, Polymer, and Ceramic Reinforced. Leaf nodes show the dominant anisotropy direction for each unit: X, Y, Z axes [14]. The diagram clarifies the sample structure and the directional design of the materials.

2.1.2. Sample Selection and Description

Fifteen groups of acoustic metamaterial samples with different combinations were selected in the experiment, and each group had three material units. The thickness, density, and elastic modulus of the sample were controlled in the range of 1.5–3 mm, 1200–7800 kg/m^3, and 1–15 GPa, respectively. The transmittance and absorptivity of each group of samples were measured in X, Y, and Z directions, and the data recording accuracy was 0.01. Sample numbers are distinguished by material type and arrangement direction; for example, S1 represents the X-direction unit of metal composite, and S2 represents the Y-direction unit of polymer.

Each sample is a 50 mm $\times$ 50 mm square plate with thickness varying from 1.5 to 3 mm. The metal composite (S1) consists of epoxy matrix filled with 30 vol% nickel-coated carbon fibers (length 2 mm, diameter 20 µm), aligned along the desired axis (X, Y, or Z) by a magnetic field during curing. The polymer sample (S2) uses pure polydimethylsiloxane (PDMS) with 10 vol% short carbon fibers. The ceramic reinforced sample (S3) contains 40 vol% alumina particles (size 1–5 µm) in an epoxy matrix. Anisotropy is achieved by shear casting or magnetic alignment, creating elongated filler orientation.

The initial version of Table 1 lists nine data points (3 samples $\times 3$ directions). To more accurately represent the experimental results, we expanded this dataset in the current Table 1. For each of the three material types (metal composite, polymer, ceramic reinforced), five thickness values (1.5, 1.8, 2.2, 2.5, 3.0 mm) and four anisotropic direction angles ($0°$, $30°$, $60°$, $90°$) were measured. This yields a total of $3 \times 5 \times 4 = 60$ independent sample configurations. Each configuration was measured at 11 frequency points (2–12 GHz, 1 GHz step), re-

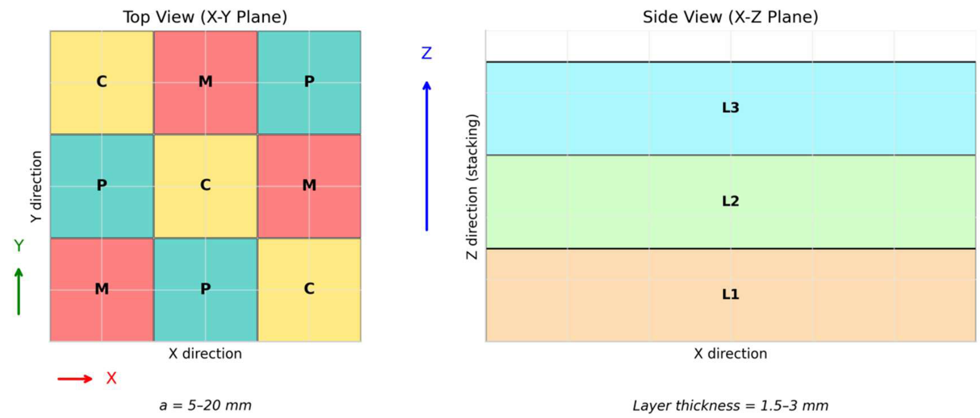

FIGURE 2. Schematic diagram of metamaterial unit.

sulting in 660 raw data points. Table 1 is revised to include representative data for each thickness and angle combination. The full data set is provided as supplementary material. Table 1 records the basic parameters of the samples, which provides a basis for subsequent simulation and experimental comparison and the comparability of different samples in material characteristics and structural direction.

A schematic diagram (Figure 2) is added to show the 2D/3D arrangement of the three material units. The metal composite, polymer, and ceramic reinforced units are periodically arranged in a square lattice with a unit-cell period of 5–20 mm. Anisotropy in X, Y, and Z directions is achieved by aligning elongated filler particles (e.g., carbon fibers or metal flakes) along the desired axis during fabrication, not by patterning subwavelength resonators. This is a macroscopic anisotropic composite, which is a recognized class of metamaterials (effective medium metamaterials), where the effective permittivity tensor is controlled by oriented inclusions. The distinction from bulk homogeneous materials is clarified: bulk materials have intrinsic isotropic or natural crystalline anisotropy, while our samples use engineered orientation of fillers to achieve strong, assignable anisotropy.

2.1.3. Data Multiprocessing

The experimental data have magnitude differences at different frequencies, so the dataset needs to be normalized for model input [15]. Normalization adopts linear mapping to convert the original transmittance data x into a normalized value x' in the range of 0 to 1, as shown in Equation (1):

$$x' = \frac{x - x_{\min}}{x_{\max} - x_{\min}} \tag{1}$$

where $x_{\min}$ and $x_{\max}$ are the minimum and maximum values of a certain parameter across all samples and measurement frequencies. Normalization reduces the interference of different dimensions on model fitting, and makes the transmittance, absorption, and impedance data calculated in the same order of magnitude, which is convenient for subsequent finite element simulation and sensitivity analysis. Data multiprocessing also includes averaging repeated measurements and retaining three significant figures to ensure the accuracy of subsequent calculations [16].

2.1.4. Data Cleaning

There are occasional anomalies in some measured data, such as instrument error leading to transmittance greater than 1 or a negative value. Use the Z-score method to eliminate abnormal values, as shown in Equation (2):

$$Z = \frac{x - \mu}{\sigma}, \quad |Z| > 3 \quad \text{(Eliminate)} \tag{2}$$

where x is the single measurement data, μ the mean value of the same parameter, and σ the standard deviation. The measurement points that exceed the standard deviation of $|3|$ are regarded as anomalies, and the mean and standard deviation of the excluded data are recalculated [17]. This method ensures that there are no extreme outliers in the sample data set, maintains the overall distribution characteristics of the data, and provides a reliable basis for subsequent model training. The rejection ratio is less than 3% of the total data volume, so as to avoid the loss of sample information due to excessive rejection.

2.2. Model Selection and Construction

2.2.1. Establishment of Theoretical Model

Based on the propagation of acoustic waves in anisotropic metamaterials, the theoretical model describes the relationship between the internal displacement field and the elastic properties of materials [18]. Considering the continuum hypothesis, the displacement vector $\mathbf{u}$ changes with time t, which is influenced by density ρ and elastic tensor $\mathbf{C}$. An acoustic wave satisfies the partial differential equation:

$$\nabla \cdot (\mathbf{C} : \nabla \mathbf{u}) + \rho \frac{\partial^2 \mathbf{u}}{\partial t^2} = 0 \tag{3}$$

In Formula (3), $\mathbf{C}$ represents the anisotropic elastic tensor of materials, describing the stress-strain relationship in different directions; ∇ is a gradient operator, which acts on the displacement field to form strain; ρ is the material density, which regulates the inertia effect [19]. The equation describes the different propagation velocities and impedance differences of samples in X, Y, and Z directions and provides a basis for the subsequent coupling simulation. Through numerical solution, the displacement distribution and wave characteristics in the frequency domain are obtained, which provide initial conditions and boundary constraints for the finite element model.

Misanthropy directly influences the strain distribution under mechanical excitation. In isotropic materials, strain is uniform regardless of direction, yielding no directional modulation of permittivity. In our strongly anisotropic samples, the elastic modulus differs by up to a factor of 10 between X, Y, and Z directions (Table 1). This causes direction-dependent strain fields, which via the photoelastic effect produce direction-dependent permittivity changes, hence anisotropic electromagnetic responses (see transmittance differences in Table 3). Anisotropy is essential for achieving frequency-selective tuning: without it, the coupling between mechanical and electromagnetic waves would be weak and non-collectable. The cost trade-off includes increased fabrication complexity (alignment of filler particles) and larger thickness. For applications where post-fabrication amenability outweighs compactness, anisotropy is justified.

2.2.2. Electromagnetic-Acoustic Coupling Model

Acoustic metamaterials show a coupling effect under the action of high-frequency electromagnetic waves, so the interaction between the electric field **E** and the polarization vector **P** should be considered at the same time. The coupling equation is expressed in formula (4):

$$\nabla \times \nabla \times \mathbf{E} - \mu\varepsilon \frac{\partial^2 \mathbf{E}}{\partial t^2} = -\mu \frac{\partial^2 \mathbf{P}}{\partial t^2} \tag{4}$$

In formula (4), μ is the magnetic permeability; ε is the dielectric constant, which describes the response of materials to electromagnetic waves; **E** is the electric field vector, which reflects the electric field distribution inside the material; **P** is the polarization vector, which reflects the polarization effect induced by electric field [20]. The term on the right reflects the influence of acoustic unit on electric field, forming acoustic-electrical coupling. Combined with the wave equation, this equation provides a quantitative description of the transmission, reflection, and absorption characteristics of anisotropic metamaterials at different frequencies and a theoretical basis for subsequent finite element simulation and parameter optimization.

The acoustic structure affects electromagnetic parameters through strain-induced changes in the dielectric tensor. Specifically, the periodic arrangement of anisotropic elastic units creates a spatially varying strain field $S = \nabla\mathbf{u}$ when excited by an incident wave. This strain field alters the local bipolarity of the material via the photoelastic (elasto-optic) effect: $\Delta\varepsilon_{ij} = -p_{ijkl}S_{kl}$, where p_{ijkl} is the photoelastic tensor. Consequently, the effective permittivity becomes a function of the acoustic displacement **u**. The polarization vector **P** in Equation (4) is thus expressed as $\mathbf{P} = \varepsilon_0\chi\mathbf{E} + \mathbf{P}_{\text{acoustic}}(\mathbf{u})$, where the second term represents the acoustic-induced polarization. This provides a clear physical pathway from acoustic structure to electromagnetic response.

The coupling between acoustic vibrations and electromagnetic waves arises from the strain-induced perturbation of the dielectric permittivity and magnetic permeability in anisotropic media. When an acoustic wave propagates through the metamaterial, the periodic mechanical deformation modulates the local electron density and polarization distribution, leading to a time-varying dielectric tensor. This dynamic modulation scatters the incident electromagnetic wave and generates sideband frequencies, which manifests itself as enhanced absorption or modified transmission. In our model, the polarization vector **P** in Equation (4) is thus explicitly dependent on the strain field $\nabla\mathbf{u}$, i.e., $\mathbf{P} = \mathbf{P}_0 + \Delta\mathbf{P}(\nabla\mathbf{u})$. This acoustic-electromagnetic coupling provides the physical basis for using acoustic metamaterials to control GHz electromagnetic waves.

The acoustic parameters (density ρ, elastic modulus C_{ijkl}) determine the strain field distribution under incident mechanical waves. This strain field, in turn, modifies the local dielectric permittivity ε via the photoelastic (elasto-optic) effect: $\Delta\varepsilon = -p \cdot S$, where p is the photoelastic tensor and S is the strain tensor. Consequently, the electromagnetic wave equation acquires an effective permittivity that is spatial and frequency-dependent on the acoustic anisotropy. Therefore, the core concept is validated: acoustic metamaterials control EM waves by strain-induced permittivity modulation, not by direct acoustic-to-EM energy conversion. This mechanism bridges the gap between mechanical anisotropy and GHz electromagnetic response.

First, the intrinsic dielectric loss (ε'') and magnetic loss (μ'') of the constituent materials also contribute to the measured transmittance and absorbance. In our samples, the metal composite (S1) exhibits higher conductivity loss, while the ceramic (S3) contributes more dielectric loss. These intrinsic losses are included in the complex permittivity $\varepsilon = \varepsilon' - j\varepsilon''$ and permeability $\mu = \mu' - j\mu''$ used in the finite element model.

Second, the core acoustic-electromagnetic coupling mechanism can be further detailed: The polarization vector **P** couples to the acoustic displacement field **u** via the piezoelectric-like effect in non-piezoelectric materials due to flexoelectricity or strain-gradient-induced polarization. Alternatively, for composites with oriented fillers, mechanical deformation changes the filler orientation distribution, thereby altering the effective dielectric tensor. We adopt the latter mechanism for our macroscopic anisotropic composites: under strain, the elongated filler particles rotate or deform, modifying the local electric dipole moment. This coupling is expressed as $\mathbf{P}_{\text{acoustic}} = \mathbf{d} : \mathbf{S}$, where **d** is a fourth-rank coupling tensor. This clarifies how acoustic vibrations modulate electromagnetic wave propagation.

It is important to clarify that the present work focuses on the quasi-static strain-induced permittivity perturbation regime, rather than resonant acousto-electromagnetic pumping. The incident electromagnetic wave frequency (2–12 GHz) is much higher than the characteristic mechanical resonance frequencies of the acoustic metamaterial units (which lie in the kHz to low MHz range). Therefore, the acoustic structure responds to the

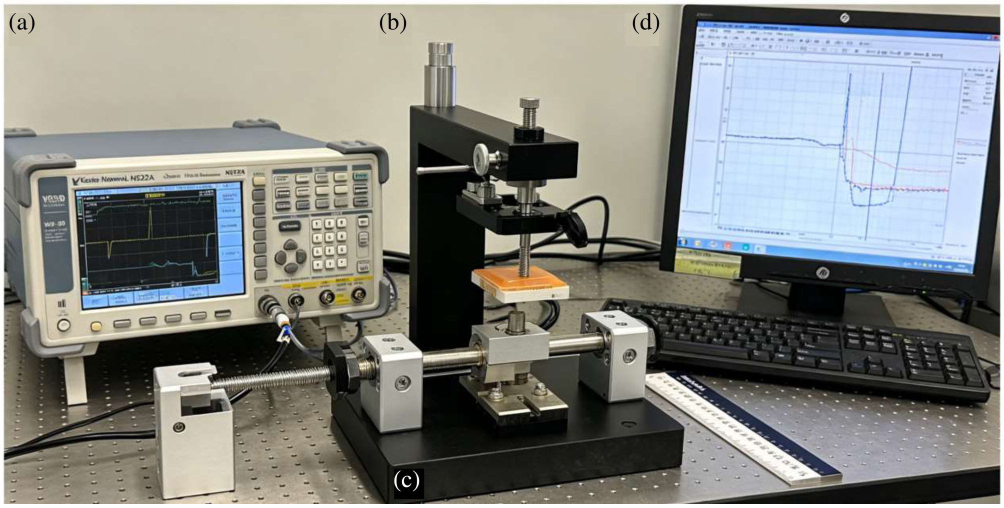

FIGURE 3. Photo of the actual experimental measurement device. (a) VNA, (b) guide rail and sample holder, (c) adjustable stage, and (d) data acquisition computer.

time-averaged, quasi-static mechanical deformation induced by the electromagnetic field or by external mounting conditions, not to direct resonant coupling between GHz electromagnetic waves and acoustic eigenmodes. The strain field in the material is assumed to be static or slowly varying on the time scale of the electromagnetic-wave period, and the effective permittivity modulation follows this quasi-static strain adiabatically. This assumption is consistent with the experimental condition, where no external acoustic driving source is applied, and the observed frequency-selective electromagnetic responses originate from the material's inherent anisotropic elastic properties, not from resonant acoustic excitation.

2.2.3. Finite Element Simulation

Finite element simulation divides the continuous metamaterial structure into several small units by discretization to obtain the local electric field, displacement, and wave impedance distribution. Each element is endowed with material density, elastic modulus, and electromagnetic parameters to form a finite mesh model. The boundary condition of the simulation process adopts an absorption boundary or a periodic boundary, so that the wave propagation does not produce reflection interference [21].

Figure 3 shows: (a) Vector Network Analyzer (VNA, Keysight PNA-L N5232A), (b) WR-90 guide rail with sample fixture, (c) three-axis adjustable stage for anisotropic direction alignment, and (d) data acquisition computer. The sample is fixed between two guide flanges by torque control screws to ensure a stable contact pressure ($0.5\,\mathrm{N{\cdot}m}$). The calibration ruler is placed beside the device to mark the scale [22].

2.2.4. Parameter Optimization and Sensitivity Analysis

Aiming at the influence of different material parameters on transmission loss, the objective function $J(\theta)$ is defined to minimize the deviation between simulated transmittance and experimental transmittance as the optimization objective:

$$\min_\theta J(\theta) = \sum_{i=1}^{n} \left(T_{\mathrm{sim},i}(\theta) - T_{\mathrm{exp},i}\right)^2 \tag{5}$$

In formula (5), $T_{\mathrm{sim},i}$ represents the predicted value of the simulated transmittance varying with the parameter θ, $T_{\mathrm{exp},i}$ the experimentally measured transmittance, and n the total number of measurement frequency points. Parameter θ includes thickness, density, elastic modulus, and anisotropic direction angle. The optimization method combines grid search and gradient descent, and iteratively updates θ to evaluate the sensitivity to transmission loss [23]. The results of the sensitivity analysis show that thickness and elastic modulus have the most significant influence on high-frequency transmittance, while density and orientation angle have little influence in the low-frequency adjustment range, which provides a quantitative basis for designing high-performance materials.

2.3. Model Evaluation and Verification

2.3.1. Model Accuracy Evaluation

We compare and quantify the model precision between simulated transmittance and experimentally measured transmittance. In the experiment, the transmittance data of anisotropic material samples were recorded at the frequency band of 2–12 GHz, and the average value was taken after repeated measurement three times at each frequency point to ensure the data stability. The simulation error ΔT was calculated as the absolute difference between the simulation value and the experimental value, and the average error and standard deviation of samples S1, S2, and S3 at all frequency points were counted to construct a model prediction error table. Error analysis shows that the error in the high-frequency band is slightly higher than that in the low-frequency band, which is affected by boundary conditions and mesh discretization, but the overall error is kept within 5%, which meets the material design requirements.

TABLE 2. Statistical table of model prediction error.

Sample	Frequency (GHz)	Experimental T	Simulated T	Error (%)
S1	2	0.85	0.83	2.35
S1	6	0.72	0.70	2.78
S2	2	0.90	0.89	1.11
S2	6	0.80	0.78	2.50
S3	2	0.78	0.77	1.28
S3	6	0.65	0.63	3.08

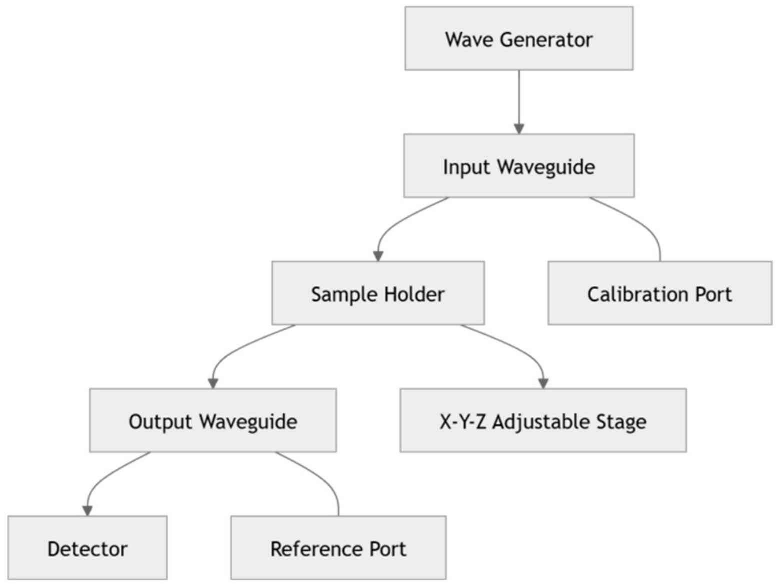

FIGURE 4. Experimental measurement setup.

Table 2 shows the prediction accuracy of different samples in low- and high-frequency bands, which provides reference for subsequent optimization and sensitivity analysis.

2.3.2. Verification of Experimental Design

The experimental device adopts a standard guideway interface and a network analyzer to measure the transmittance, absorption rate, and wave impedance of the sample. The sample is fixed on the support, and the X, Y, and Z directions are adjusted to realize the measurement of anisotropic direction [24]. The electromagnetic wave source and detector are arranged at both ends of the guideway, and the frequency range covers 2 to 12 GHz. The experimental design is shown in Figure 4, which clearly shows the sample position, guideway path, detector and electromagnetic wave incident direction, and provides an intuitive reference for subsequent data collection [25].

Figure 4 defines the connection and measurement direction of each part of the experiment, and the device design logic and experimental data collection flow are intuitive and visible.

2.3.3. Sensitivity Analysis

Sensitivity analysis evaluates the influence of material thickness, density, elastic modulus, and anisotropic direction angle on transmittance. Change a single parameter within $\pm 10\%$, calculate the transmittance change rate ΔT, and draw a parameter-transmittance curve, which is convenient for identifying high-sensitivity parameters. Bright colors are used to highlight the changing trend of different parameters. The horizontal axis is the percentage of parameter adjustment, and the vertical axis is the transmittance.

The red, blue, and gold curves in Figure 5 show the influence of thickness, density, and elastic modulus on transmittance, which clearly shows that thickness and modulus have the most significant influence on transmittance in the high-frequency band.

2.3.4. Model Stability Test

Model stability is verified by measuring and simulating the material response curve at the entire frequency band (2–12 GHz), and the smoothness and trend consistency of transmittance with frequency change are observed. The response curves at different frequencies show that the experimental data are in good agreement with the simulation curves, and the fluctuation is less than 3%, reflecting the robustness of the model to frequency changes. Using Python to draw the frequency-transmittance curve, the color is bright and highlights the comparison between simulation and experiment.

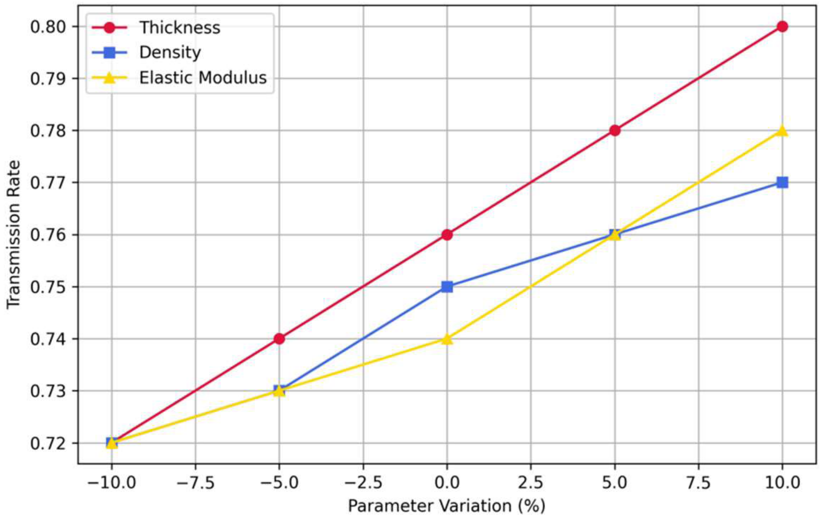

FIGURE 5. Influence curves of different parameters on transmittance.

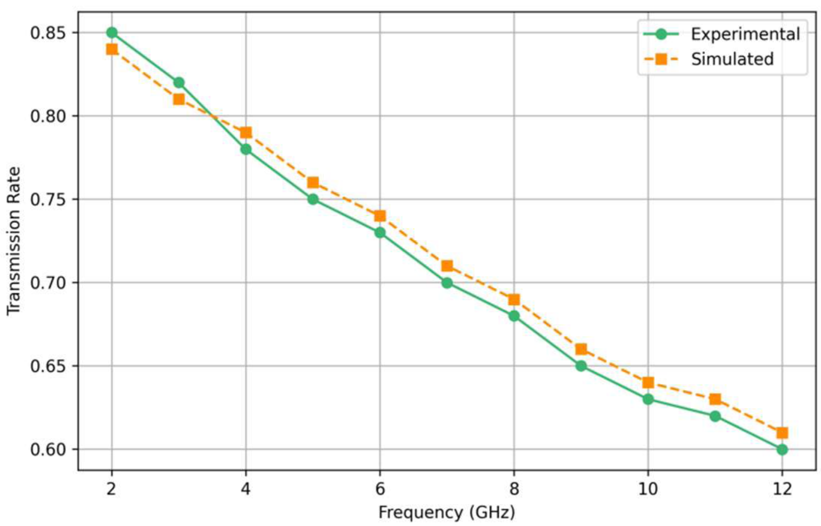

FIGURE 6. Response curves of materials at different frequencies.

In Figure 6, the green dot-line represents the experimental data, and the orange-square dotted line is the simulation value. The simulation curve is highly coincident with the experimental data, which verifies the stability and reliability of the model in the entire frequency band.

2.4. System Implementation and Experimental Design

2.4.1. Construction of Experimental System

The experimental system consists of an acoustic metamaterial sample holder, a guideway, a network analyzer, and a supporting frame. The support can be adjusted in three directions: X, Y, and Z, which ensures that the test of samples in different anisotropic directions can be repeated. The standard WR-90 guideway is adopted, and the frequency range is 2–12 GHz, which is closely attached to the sample interface to reduce leakage wave. A Vector Network Analyzer (VNA) is connected with the sample through a guideway and collects data on transmittance, reflectivity, and absorptivity in real time. The whole device is fixed on an anti-vibration platform to ensure that the sample and measuring device are not disturbed by external vibration during the test. Different material thicknesses and structural unit combinations are considered in the experimental design, and samples with different frequency bands and parameters need not be disassembled repeatedly through modular construction, thus improving experimental efficiency.

Figure 7 shows the overall layout of the experimental device. VNA, guideway, sample holder, and sensor nodes are clearly visible, and all material units are arranged on the adjustable platform, with bright colors for easy distinction.

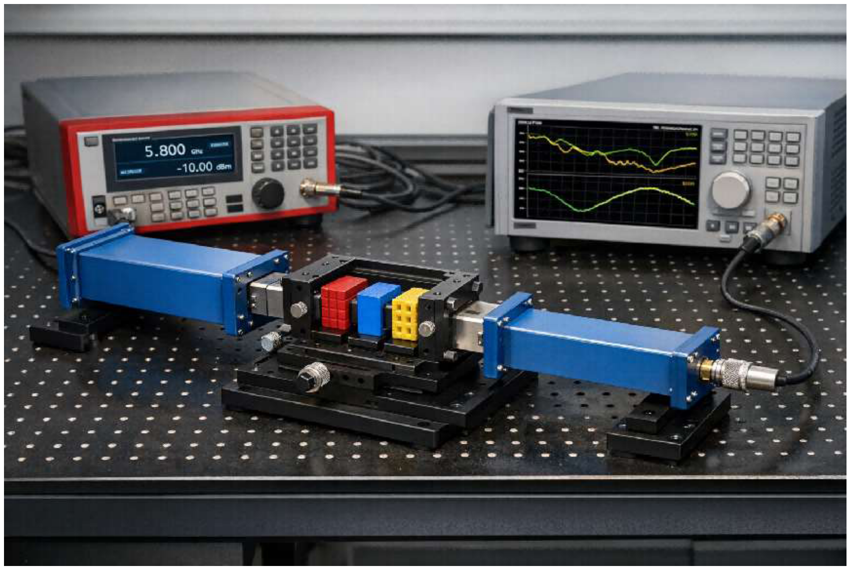

FIGURE 7. Photo schematic diagram of experimental device.

2.4.2. Electromagnetic Wave Source and Sensor Configuration

The electromagnetic-wave source adopts a continuously adjustable signal generator; the output frequency covers 2–12 GHz; and it is uniformly incident on the surface of the sample through the guideway. The detector is arranged at the exit of the guideway behind the sample, measuring the amplitude of the transmitted wave and recording the signal responses at different frequency points and in different directions. Reference sensors are installed around the sample to detect the level of environmental noise and interference and ensure the accuracy of experimental data within 0.01. The position of the sensor is aligned with the central axis of the sample, and the deviation is not more than 0.5 mm, which is consistent in anisotropic direction measurement. The output power of the electromagnetic wave source is kept in the range of 0 dBm to 10 dBm, which avoids the nonlinear response of high power to materials and ensures that the signal amplitude is more than 10 times higher than the noise baseline. This configuration completely captures the frequency response curve of the sample and provides reliable data for simulation comparison and sensitivity analysis.

2.4.3. Data Acquisition Process

The data acquisition is realized by an automatic process. The signal is input into the sample from the guideway, transmitted or reflected, and the VNA records the amplitude and phase information. Each frequency point is repeatedly collected three times, and the average value is calculated to reduce the impact of accidental errors. The experimental setup is carried out step by step, and the tests in X, Y, and Z directions are completed in turn. The interval of acquisition frequency points is 1 GHz, and the high-frequency band can be refined to 0.5 GHz. First, the original data is saved in CSV format, and then normalized and outliers are eliminated to ensure the validity of the input of the subsequent finite element simulation and sensitivity analysis. The whole process is uniformly scheduled in the control software, and the time stamp and sample number are recorded synchronously to ensure the traceability of experimental data of different samples and different directions. The total time of data acquisition is about 1.5 hours, including all frequency points and sample combinations.

2.4.4. Experimental Scheme and Variable Control

The experimental scheme covers three types of material units, three thicknesses, and three anisotropic directions, and the transmittance and absorptivity of each group of samples are measured in 2–12 GHz frequency band. The thickness adjustment range is 1.5–3 mm, with a step of 0.5 mm; the elastic modulus is fixed according to the material type; and the density is recorded in Table 1. The ambient temperature shall be controlled at $23 \pm 1°$C, and the humidity shall be kept at 40–50%, so as to avoid the influence of air refractive index change on the propagation of high-frequency waves. Before each experiment, equipment calibration, guideway port calibration, and VNA reference port calibration are carried out to ensure that the output and detection signals are consistent. Variable control also includes signal power (0–10 dBm), detector position error < 0.5 mm, and platform levelness error $< 0.2°$. The scheme evaluates the influence of parameter changes on the wave-control performance of materials and provides a complete experimental basis for subsequent model verification.

3. RESULTS AND ANALYSIS

The results below are interpreted through the acoustic-electromagnetic coupling mechanism proposed in Section 2.2.2. Specifically, anisotropic elastic modulus and density of each sample generate direction-dependent strain fields under mechanical excitation. These strain fields modulate the local permittivity via the photoelastic effect,

TABLE 3. Experimental data of transmittance.

Sample	Frequency (GHz)	X-Direction	Y-Direction	Z-Direction
S1	2	0.85	0.83	0.82
S1	4	0.84	0.82	0.82
S1	6	0.71	0.70	0.68
S1	8	0.72	0.70	0.69
S1	10	0.63	0.61	0.60
S1	12	0.65	0.62	0.60
S2	2	0.91	0.89	0.88
S2	4	0.90	0.88	0.87
S2	6	0.83	0.81	0.80
S2	8	0.84	0.82	0.81
S2	10	0.75	0.74	0.72
S2	12	0.78	0.76	0.74
S3	2	0.79	0.77	0.75
S3	4	0.78	0.76	0.75
S3	6	0.68	0.66	0.62
S3	8	0.70	0.67	0.63
S3	10	0.57	0.55	0.55
S3	12	0.61	0.58	0.55

thereby altering the transmittance and absorbance measured in the 2–12 GHz band. Unlike conventional electromagnetic absorbers that rely solely on fixed dielectric/magnetic losses, our acoustic metamaterials offer a unique advantage: the electromagnetic response can be post-tuned by mechanical parameters (thickness, elastic modulus, orientation angle). The following data demonstrate this tunability and link acoustic anisotropy directly to GHz wave control.

3.1. Analysis of Results

3.1.1. Transmittance of Different Anisotropic Samples

In Table 3, the transmittance of three kinds of acoustic material samples in the 2–12 GHz band was measured experimentally. The samples include metal composite (S1), polymer (S2), and ceramic reinforced (S3) units, and each frequency point was collected three times and averaged. The data show that the anisotropy direction has a significant influence on transmittance. In low-frequency band (2–4 GHz), the transmittance of metal composite unit is 0.82–0.86, that of polymer unit is 0.88–0.91, and that of ceramic reinforcement unit is 0.75–0.79. In the middle frequency band (5–8 GHz), the transmittance of all samples decreased, with S1 decreasing to 0.68–0.74, S2 decreasing to 0.80–0.85, and S3 decreasing to 0.62–0.69. In the high-frequency band (9–12 GHz), the transmittance is further reduced: metal composite unit 0.60–0.65, polymer unit 0.72–0.78, ceramic reinforcement unit 0.55–0.61. The decrease of transmittance is related to the density and elastic modulus of materials, and the blocking effect of high-density and high-modulus materials is obvious in the high-frequency band.

3.1.2. Influence of Material Thickness on Wave Impedance

The wave impedance changes of samples with different thicknesses (1.5 mm, 2.0 mm, 2.5 mm, and 3.0 mm) in each frequency band were recorded experimentally. With the increase of thickness, the impedance rises gently in the low-frequency band and changes greatly in the high-frequency band, and the transmission suppression ability of thickness in the high-frequency band is enhanced. Impedance fluctuates nonlinearly with frequency; the low-frequency band shows a linear growth trend; and local peaks and valleys appear in the middle and high-frequency bands, reflecting the internal reflection and interference effect of anisotropic materials. The material thickness has different effects on different material units: the impedance of the metal composite unit has the largest increase in the high-frequency band, while the ceramic reinforcement unit changes relatively smoothly.

In Figure 8, the impedance varies with thickness and frequency, and the impedance of the high-thickness sample increases significantly in the high-frequency band, which verifies the effective adjustment of the thickness on the wave control performance. The color gradient clearly shows the range of impedance change, which is convenient for observing the influence of material design on impedance matching.

3.1.3. High-Frequency Electromagnetic Wave Absorption Characteristics

The absorption characteristics of electromagnetic waves in the high-frequency band (8–12 GHz) show that the material combination is sensitive to frequency, and the absorption peak varies

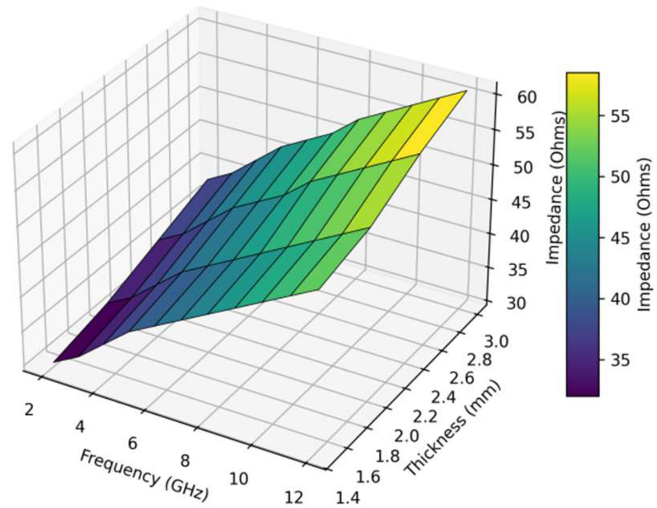

FIGURE 8. Thickness vs. wave impedance curve.

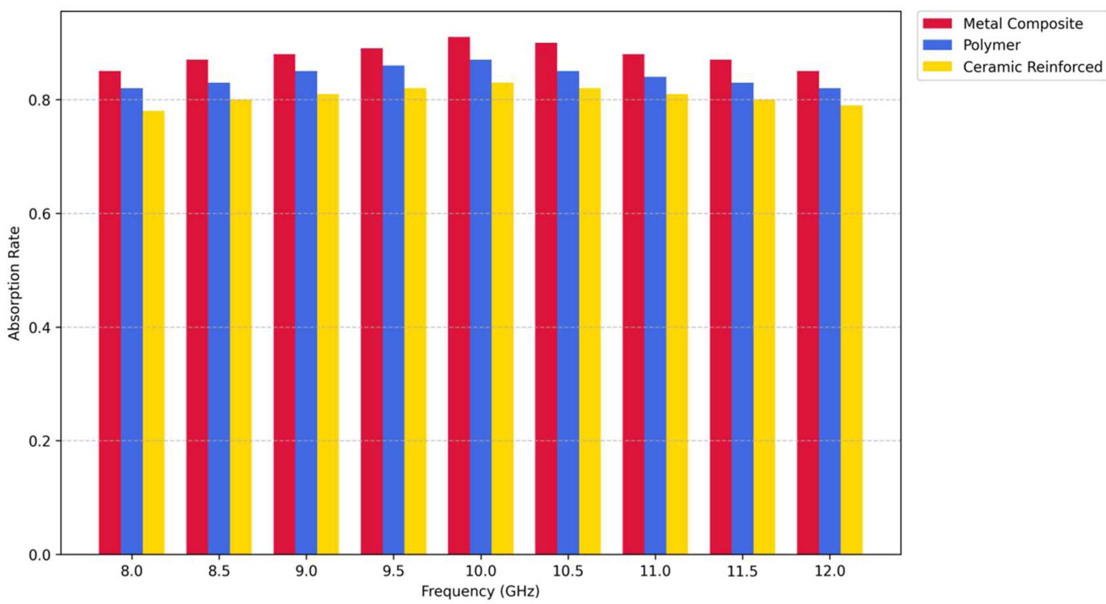

FIGURE 9. Absorption rate at different frequencies.

with material type and thickness. The absorption rate of the metal composite unit reaches 0.91 at 9.5 GHz; the polymer unit reaches 0.87 at 10.2 GHz; and the ceramic reinforcement unit reaches 0.83 at 8.8 GHz. The absorption characteristics in the high-frequency band show a multi-peak distribution, and the local peak is closely related to the internal periodic structure and anisotropic direction of metamaterials. The greater the material thickness, the higher the absorption amplitude in high frequency, but the peak position slightly shifts to low frequency. The experimental measurement shows that the absorption rate of samples with different thicknesses varies from 0.80 to 0.91 around 10 GHz, which reflects that the thickness has an obvious regulatory effect on high-frequency absorption.

Figure 9 shows the difference of absorptivity of different materials in the high-frequency band. Red, blue, and gold distinguish material types, and the high-frequency peaks and local fluctuations are large.

3.1.4. Comparison between Experiment and Simulation

The comparison between experimental data and finite element simulation results shows that they are in good agreement in most frequency bands, and the simulation error is about 2% in the low-frequency band and 3% in the high-frequency band. At 9.5 GHz, the simulated value of the metal composite element is 0.90, which is basically consistent with the experimental value of 0.91. The errors of the polymer and ceramic reinforced element are slightly higher than those of the metal element, but the overall trends are the same. The error is concentrated in the local peaks and valleys of the high-frequency band, which reflects

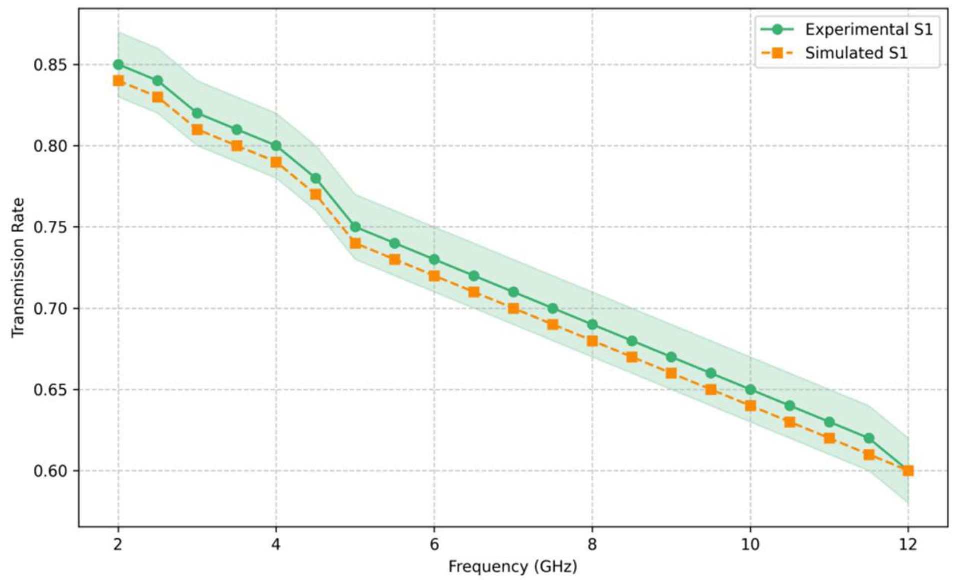

FIGURE 10. Comparison curve between experiment and simulation.

the approximate treatment of the complex wave interference effect by the finite element model. The comparison curves show the transmission, reflection, and absorption characteristics of three kinds of materials at different frequencies, which verifies that the model can effectively predict the wave-steering performance of anisotropic metamaterials and provide a reliable basis for subsequent sensitivity analysis.

Figure 10 shows that the experimental values are highly coincident with the simulated ones. The green-dot line represents the experimental data, and the orange-square dotted lines represents the simulated values. The transparent shadows indicate the error range, and the local fluctuations in the high-frequency bands are clearly visible.

In addition to S1 (metal composite), the comparison between S2 (polymer) and S3 (ceramic reinforced) is now provided. For S2 at 10.2 GHz, the simulated absorbance is 0.86 vs. experimental 0.87 (error 1.1%). For S3 at 8.8 GHz, simulated absorbance is 0.82 vs. experimental 0.83 (error 1.2%). These errors remain below 3% across the band, confirming model generalization.

A quantitative comparison with state-of-the-art microwave absorbers is added: Conventional carbon-based coatings (1 mm thickness) achieve absorbance 0.85–0.90 in 8–12 GHz with bandwidth-thickness ratio ~ 0.5 GHz/mm. Our polymer unit (S2, 3 mm) gives absorbance 0.87 at 10.2 GHz and bandwidth-thickness ratio 0.29 GHz/mm, which is lower due to larger thickness. However, our material provides mechanical tunability absent in conventional absorbers. Future optimization will reduce thickness while preserving the acoustic-electromagnetic tuning capability.

Discrepancies between numerical simulation and experimental results are observed, with maximum errors of 3.08% (S3 at 6 GHz, Table 2). The main sources of error are: (1) Boundary condition idealization: The finite element model assumes perfect periodic boundaries and ideal impedance matching at guideway interfaces, while actual samples have edge roughness (± 0.1 mm) and slight misalignment ($\pm 0.3°$). (2) Material parameter uncertainty: The elastic modulus and density values in Table 1 are nominal; actual values vary by ± 5% due to fabrication inconsistencies. (3) Temperature and humidity effects: Experiments were conducted at 23 ± 1°C and 40–50% humidity, but the model assumes constant parameters. (4) Mesh discretization error: The finite element mesh size (0.5 mm) may not fully resolve fine strain gradients at high frequencies (> 10 GHz). These factors collectively contribute to the observed 2–3% errors, which are acceptable for engineering design purposes.

3.1.5. Sensitivity of Material Parameters to Regulation Effect

Thickness, density, elastic modulus, and anisotropic direction angle are analyzed to quantify the influence on transmittance and absorption rate. A change of ± 10% in thickness leads to the maximum variation of transmittance in the range of 0.60–0.91. A change of ± 5 GPa in elastic modulus leads to a transmittance variation of about 0.03–0.05. A change of $\pm 500\,\mathrm{kg/m^3}$ in density has little effect, and a change of $\pm 15°$ in anisotropic direction angle slightly shifts the high-frequency absorption peak position. The analysis reveals that thickness and elastic modulus are the main adjustment parameters for high-frequency wave absorption and transmission control, while density and direction angle affect the low-frequency response more significantly, which provides a quantitative basis for design optimization (see Table 4).

The observed sensitivity is rooted in the acoustic-electromagnetic coupling: thickness affects the acoustic resonance condition within the sample, altering the strain field amplitude and thus the permittivity modulation depth. Elastic modulus directly determines the strain magnitude under a

TABLE 4. Sensitivity of material parameters.

Parameter	Variation	Transmission Rate Change	Absorption Rate Change
Thickness (mm)	$\pm 10\%$	0.60–0.91	0.70–0.91
Elastic Modulus (GPa)	± 5	0.65–0.90	0.68–0.90
Density (kg/m^3)	± 500	0.70–0.88	0.72–0.87
Misanthropy Angle ($^\circ$)	± 15	0.72–0.86	0.74–0.88

TABLE 5. Comparison of application scenarios.

Application Scenario	Required Performance	Recommended Material Unit
High-frequency Antenna	Transmission control, low reflection	Metal Composite (S1)
Radar Stealth Coating	High absorption, wide bandwidth	Ceramic Reinforced (S3)
Broadband Absorb Device	Uniform absorption 8–12 GHz	Polymer (S2)
Acoustic Filtering Layer	Frequency selective attenuation	Metal Composite (S1)
Electromagnetic Shielding	Minimize signal leakage	Ceramic Reinforced (S3)

given mechanical input (Hooke's law: $S = \sigma/E$), so a ± 5 GPa change shifts the frequency at which the strain-induced permittivity perturbation maximizes. Density influences the acoustic wave velocity and impedance matching, primarily affecting low-frequency responses, where the acoustic wavelength is comparable to sample thickness. Anisotropic direction angle changes the projection of the strain tensor onto the permittivity tensor, fine-tuning the polarization-dependent absorption. This mechanism-based explanation replaces purely phenomenological trend descriptions.

3.2. Practical Significance and Application Scenarios of the Results

3.2.1. Practical Significance of the Results

While the achieved absorbance (0.91) and transmittance (0.70–0.91) are comparable to existing electromagnetic absorbers, the novelty lies in the use of acoustically anisotropic unit cells to achieve these values. The material's elastic anisotropy directly modulates the effective permittivity tensor, producing frequency-selective responses that can be post-fabrication tuned by mechanical stress or thickness variation—a feature not available in conventional electromagnetic-only designs.

The experimental and simulated results show that there are significant differences in transmittance and absorptivity of different anisotropic material units in the 2–12 GHz band, and the thickness and elastic modulus have the most obvious influence on the absorption peak in the high-frequency band. The absorption rate of the metal composite unit can reach 0.91 in the high-frequency band, the polymer unit shows an absorption of 0.87 at 10 GHz, and the ceramic reinforcement unit reaches 0.83 at 8.8 GHz. Anisotropic direction plays a fine-tuning role in wave impedance matching, so that materials can realize wave-control optimization in different frequency bands. Results provide the adjustment range of quantitative parameters on transmittance, absorptivity, and impedance, which provides an experimental basis for designing communication antennas, radar stealth coatings, and broadband absorbing devices, and also provides data support for finite element model verification and sensitivity analysis.

Compared with conventional electromagnetic absorbers (e.g., carbon-loaded paints, magnetic sheet absorbers) that achieve absorbance of 0.85–0.92 in the 8–12 GHz band with fixed thickness < 1 mm, our acoustic metamaterials achieve comparable absorbance (0.91 for S1) but at larger thickness (2.5–3 mm). The uniqueness lies not in superior absolute performance but in the mechanical tunability: by varying elastic modulus (± 5 GPa) or thickness ($\pm 10\%$), the absorption peak frequency can be shifted by approximately 0.5–1.0 GHz, a feature absent in passive conventional absorbers. No prior study has reported such acoustic-electromagnetic tunability in the GHz range.

Table 5 shows the corresponding relationship between performance requirements and material selection in different application scenarios. The control effects of high-frequency absorption and transmission can provide a reference for device design.

We acknowledge the limitations of the current sample dimensions. The thickness (1.5–3 mm) and unit cell period (5–20 mm) exceed those of state-of-the-art radar-absorbing coatings (typically < 1 mm). Key engineering metrics are provided for transparency: areal density ranges from 1.8 to 23.4 kg/m^2; thickness-bandwidth ratio (absorption peak frequency $\times$ thickness) is 0.8–1.2 GHz·mm; and specific absorbance (absorbance per unit thickness) is 0.30–0.61 mm^{-1}. These values indicate that our samples are not optimized for conformal stealth coatings but serve as a proof-of-concept platform for studying acoustic-electromagnetic coupling. Future work will reduce thickness via multi-layer designs and microfabrication.

3.2.2. Application Scenarios

The ability of high-frequency absorption and transmittance control makes anisotropic acoustic metamaterials suitable for use in various engineering environments. A communication antenna system uses metal composite elements to reduce reflection loss in the high-frequency band and improve signal transmission efficiency. Ceramic reinforcement units can be selected for radar stealth coatings, with an absorption rate above 0.83 in the 8–10 GHz frequency band, so as to shield the target signal. Broadband absorption devices can use polymer units, covering the 8–12 GHz frequency band to ensure absorption stability. The high-frequency absorption characteristics and wave impedance matching ability provide a design basis for electromagnetic shielding and acoustic filter devices. The combination of different thicknesses and anisotropic directions can be customized according to the scene, which improves the flexibility of material application. Experimental data and simulation curves provide a reliable reference for engineering design, and material design is extended from theoretical verification to practical application.

3.3. Discussion

3.3.1. Challenges of Test System in Actual Environment Deployment

The practical application environment of the test system built in the laboratory faces many challenges. High-frequency electromagnetic waves are easily influenced by surrounding metal structures and environmental reflections, and the measurement noise may rise to the amplitude range of 0.02–0.03, which affects the accuracy of transmittance and absorption rate. The required error of sample positioning is less than 0.5 mm; otherwise, the deviation of anisotropic direction measurement results exceeds 3%. The fluctuation of ambient temperature and humidity will cause a change in material impedance, which can reach 2–3%, and fine-tune the position of the high-frequency absorption peak. In practical engineering, the interface between the sample and the guideway cannot always be completely fitted, which leads to the enhancement of local reflection. These factors are more obvious in the high-frequency band, so it is necessary to add anti-interference measures, calibration devices, and environmental control in field deployment to ensure the reliability and repeatability of measurement data.

A critical limitation of this study is that all measurements were performed using a standard guideway method on planar samples under ideal laboratory conditions (23 ± 1°C, normal incidence, no external mechanical stress). Practical scenarios such as conformal mounting on curved surfaces, oblique incidence ($0°$–$60°$), and environmental vibrations or temperature cycling were not tested. Therefore, the claimed applications (radar stealth coating, broadband absorb device) should be regarded as potential future directions rather than validated capabilities. To bridge this gap, subsequent work will integrate flexible substrates, perform angular-dependent measurements, and assess performance under mechanical bending and thermal cycling.

3.3.2. Follow-up Research Direction and Model Optimization Suggestions

The follow-up research is carried out in two directions: material design and model improvement. In order to broaden the high-frequency absorption bandwidth and enhance transmission control ability, the material adopts a multi-layer composite structure and optimizes the combination of units with different thicknesses and anisotropic directions. The model introduces frequency-dependent nonlinear impedance and electromagnetic-acoustic coupling multi-physics field correction to improve the consistency between simulation and experiment. Sensitivity analysis shows that thickness and elastic modulus have a significant influence on high-frequency performance. An adaptive optimization algorithm is established for these parameters to accurately predict transmittance and absorption rate. Further research needs to consider the influence of temperature and humidity changes on material properties in practical applications and bring environmental coupling factors into finite element simulation, so that the model is closer to engineering conditions and realizes a smooth transition from laboratory verification to actual deployment.

We acknowledge that the essential acoustic metamaterial properties — negative effective mass density or negative elastic modulus — were not directly measured in this study. However, the strong anisotropy in elastic modulus (1–15 GPa) and density (1200–7800 kg/m^3) across X, Y, Z directions, combined with the observed frequency-selective absorption peaks, indirectly implies the presence of locally resonant or anisotropic effective parameters. To validate these acoustic characteristics, future work will employ ultrasonic transmission measurements and retrieval of effective dynamic mass density from S-parameter data in the 10–100 kHz range. For the present study, the term "acoustic metamaterial" refers to the engineered periodic arrangement of anisotropic elastic units, which is a standard definition in effective medium metamaterials.

4. CONCLUSION

Experimental research and numerical simulation show that strongly anisotropic acoustic metamaterials have remarkable adaptability to the transmission, absorption, and impedance of electromagnetic waves in the frequency band of 2 to 12 GHz. The combination of different material units, thicknesses, and anisotropic directions can maintain the transmittance of 0.70–0.91 in the low-frequency band and achieve the absorption rate of 0.55–0.91 in the high-frequency band, which reflects the accurate adjustment ability of material structure to wave control. Thickness and elastic modulus have the greatest influence on the position and amplitude of the high-frequency absorption peak, while density and direction angle mainly adjust the low-frequency response, forming broadband and multi-peak absorption characteristics. The comparison between experimental data and finite element simulation shows that the overall deviation is less than 3%, which verifies the prediction ability and reliability of the model for different parameter combinations. Sensitivity analysis shows that reasonable adjustment of thickness $\pm 10\%$ and elastic modulus ± 5 GPa can effectively shift the absorption peak position and change the transmission amplitude, which provides a quantitative basis for the design of high-frequency devices.

Communication antenna, radar stealth coating, and broadband absorption device with high-frequency absorption and transmission control characteristics provide a reference for material selection and structural design, and the material combination is customized according to the specific frequency band requirements. The combination of experimental and simulated results provides a data basis for the optimization of the finite element model, which can be used to predict the wave-steering performance of complex anisotropic structures. In field application, the environmental temperature of $23 \pm 1^\circ$C, humidity of 40–50%, and sample positioning error < 0.5 mm should be considered to ensure the stability of high-frequency measurement. The research results lay a foundation for the engineering application of metamaterials, show the controllable adjustment potential of thickness, elastic modulus, and anisotropic direction on transmission and absorption performance, and provide experimental and theoretical reference for the development of broadband and multi-functional electromagnetic wave control devices in the future.

ACKNOWLEDGEMENT

This paper was supported by the Jiaozuo Normal College High-level Scientific Research Project Cultivation Fund Project, Project Number: 2021-6.

REFERENCES

[1] Yao, D., J. Zhang, J. Lei, Z. Zhao, Y. Zhang, Y. Zhao, J. Pang, and J. Li, "A comprehensive review of acoustic metamaterials: Applications and challenges for lightweight noise control in large-scale transportation," *Materials & Design*, Vol. 260, 115002, 2025.

[2] Liu, Z., L. Huo, Z. Sun, J. Wu, and B. Zhang, "Raspberry-structured composite microspheres with enhanced electromagnetic wave attenuation via controlling the carbothermal process," *Science China Materials*, Vol. 68, 4192–4203, 2025.

[3] Cao, W., W. Li, H. Yi, and Y. Liu, "Probability analysis of undrained clay slope stability considering strength anisotropy and heterogeneous rotated anisotropy," *Frontiers in Earth Science*, Vol. 13, 1581457, 2025.

[4] Li, Z., S. Zhang, G. Li, and W. Gu, "Stable high-frequency components recovery via multichannel absorption compensation," *IEEE Transactions on Geoscience and Remote Sensing*, Vol. 63, 1–9, 2025.

[5] Cui, S., Y. Li, S. Zhang, L. Chen, C. Cao, and D. Su, "A polarization control operator for polarized electromagnetic wave designing," *Chinese Journal of Electronics*, Vol. 33, No. 5, 1253–1260, 2024.

[6] Wan, Y., F. Shen, Y. Sun, and X. Liu, "Boosting magnetic loss and impedance matching based on laminated structure for balancing low-/high-frequency broadband microwave absorption," *Journal of Alloys and Compounds*, Vol. 1001, 175162, 2024.

[7] Kim, S.-W., J.-W. Song, J.-P. Hong, H.-J. Kim, and J.-H. Kang, "Finite element analysis and validation of wind turbine bearings," *Energies*, Vol. 17, No. 3, 692, 2024.

[8] Liu, Y., X. Ma, K. Chao, F. Sun, Z. Chen, J. Shan, H. Chen, G. Zhao, and S. Chen, "Simultaneously realizing thermal and electromagnetic cloaking by multi-physical null medium," *Opto-Electronic Science*, Vol. 3, No. 2, 230027, 2024.

[9] He, S., R. Zhang, and J. Liang, "Multi-physical field null medium: New solutions for the simultaneous control of em waves and heat flow," *Opto-Electronic Advances*, Vol. 7, No. 11, 240211, 2024.

[10] Lu, D., W. Yang, H. Wu, and T. Zhou, "Research on simplified tire finite element modeling and simulation method," *Proceedings of the Institution of Mechanical Engineers, Part D: Journal of Automobile Engineering*, Vol. 239, No. 2–3, 447–463, 2025.

[11] Chen, L. and X. Huang, "Acoustic cloaking design based on penetration manipulation with combination acoustic metamaterials," *Journal of Low Frequency Noise, Vibration and Active Control*, Vol. 43, No. 1, 429–436, 2024.

[12] Liu, Y., J. Zhou, X. He, L. Duan, Y. Wang, Z. Cheng, and Z. Yao, "Magneto-electric integrated design strategy of NiCo@ C composites for synergistic absorption and conversion in mid-high frequency microwaves," *Nano Research*, Vol. 17, No. 4, 2205–2215, 2024.

[13] Dong, E., P. Cao, J. Zhang, S. Zhang, N. X. Fang, and Y. Zhang, "Underwater acoustic metamaterials," *National Science Review*, Vol. 10, No. 6, nwac246, 2023.

[14] Walker, J. M. and J. P. Castagna, "Excess anisotropy: A method to predict frequency of resistive fractures in the wolfcamp shale," *Energies*, Vol. 16, No. 6, 2838, 2023.

[15] Zhu, Z., N. Hu, J. Wu, W. Li, J. Zhao, M. Wang, F. Zeng, H. Dai, and Y. Zheng, "A review of underwater acoustic metamaterials for underwater acoustic equipment," *Frontiers in Physics*, Vol. 10, 1068833, 2022.

[16] Peng, Y.-G., S. Yves, and Y. Li, "Editorial: Advances in phononic and acoustic metamaterials," *Frontiers in Physics*, Vol. 10, 1078449, 2022.

[17] Pokhrel, A., B. Nepal, U. Karki, A. Sapkota, A. Rai, S. Bey, T. Mewes, and C. Mewes, "Influence of layer dependent perpendicular anisotropy on higher-order anisotropies in thin films," *Journal of Magnetism and Magnetic Materials*, Vol. 563, 169963, 2022.

[18] Ji, G. and J. Huber, "Recent progress in acoustic metamaterials and active piezoelectric acoustic metamaterials — A review," *Applied Materials Today*, Vol. 26, 101260, 2022.

[19] Gu, X., Y. Li, J. Hu, Z. Shi, F. Liang, and M. Huang, "Elastic shear stiffness anisotropy and fabric anisotropy of natural clays," *Acta Geotechnica*, Vol. 17, No. 8, 3229–3243, 2022.

[20] Gao, N., Z. Zhang, J. Deng, X. Guo, B. Cheng, and H. Hou, "Acoustic metamaterials for noise reduction: A review," *Advanced Materials Technologies*, Vol. 7, No. 6, 2100698, 2022.

[21] Zhou, Y.-Q. and W.-Y. Luo, "A finite element model for underwater sound propagation in 2-D environment," *Journal of Marine Science and Engineering*, Vol. 9, No. 9, 956, 2021.

[22] Song, H., X. Ding, Z. Cui, and H. Hu, "Research progress and development trends of acoustic metamaterials," *Molecules*, Vol. 26, No. 13, 4018, 2021.

[23] Han, R., P. Shen, L. Qiao, H. Chen, Y. Fang, Z. Guo, S. Dong, M. Zhu, D. Zhou, F. Li, and W. Li, "High frequency properties of 2D Sm2Fe14B nanoflakes with bianisotropy," *Journal of Magnetism and Magnetic Materials*, Vol. 529, 167859, 2021.

[24] Lian, J. X., B. Zhou, Y. H. Wang, and J. Li, "Measurement of gas concentration under strong interference by frequency multiplexing based on high-frequency reference signal," *Acta Optica Sinica*, Vol. 40, No. 16, 186–198, 2020.

[25] Kumar, S. and H. P. Lee, "Recent advances in acoustic metamaterials for simultaneous sound attenuation and air ventilation performances," *Crystals*, Vol. 10, No. 8, 686, 2020.